Shear thickening in low-concentration solutions of wormlike micelles. II. Slip, fracture, and stability of the shear-induced phase

Y. T. Hu and Philippe Boltenhagen[a)]

Department of Chemical Engineering, University of California, Santa Barbara, California 93106-5080

Eric Matthys

Department of Mechanical Engineering, University of California, Santa Barbara, California 93106

D. J. Pine[b)]

Departments of Chemical Engineering and Materials, University of California, Santa Barbara, California 93106-5080

(Received 19 February 1998; final revision received 26 May 1998)

Synopsis

The rheology of the shear-thickened state is investigated in low-concentration solutions of wormlike micellar solutions using mechanical, optical, and velocity profile measurements. The zero-shear-rate viscosity of the solutions increases by more than a factor of 1000 as the concentration of surfactant is increased from 1 to 10 mM. By contrast, the apparent viscosity of the shear-thickened state of these same solutions is observed to be remarkably independent of concentration over a wide range of shear rates. This is shown to be a consequence of the development of slip layers between the very viscous gellike shear-induced structures (SISs) which form in the bulk of the surfactant solution and on the walls of the Couette devices in which the measurements are made. As the applied shear stress is increased even further, there is evidence that the SIS fractures give rise to a shear-rate-independent stress and an apparent viscosity, which decreases with increasing shear rate. After the SIS fractures, large fluctuations in the shear rate are observed to result from an SIS which alternately fractures, slips, heals, and refractures. The fracture stress is proportional to the concentration and inversely proportional to the cell radius. © *1998 The Society of Rheology.* [S0148-6055(98)00505-7]

I. INTRODUCTION

In the preceding article, Part I (Hu *et al.*, 1998), we investigated shear thickening in low-concentration wormlike micellar solutions using simultaneous rheological and visualization measurements. In that article, we focused on the transition from the low-viscosity to the high-viscosity state and found that transition to be similar to a phase

[a)]Present address: Laboratoire d'Ultrasons et de Dynamique des Fluides Complexes, URA au CNRS no. 851, Université Louis Pasteur-rue Blaise Pascal, 67070 Strasbourg, France.
[b)]Author to whom all correspondence should be addressed (electronic mail: pine@engineering.ucsb.edu).

transition. In this article, we focus on the rheology of the shear-thickened state, where we find a rich variety of behavior, including wall slip, fracture, and flow instabilities. We bring to bear on these problems the same experimental tools as in the previous article, Part I, namely rheological measurements and visualization of the shear-induced structures. To those we also add measurements of the velocity profile. Using these techniques we are able to shed light on some fairly long-standing puzzles in these systems, particularly with respect to previously reported dependence of the rheological properties on the geometry of the flow cells.

In the preceding article, Part I, we identified four regimes of flow behavior in these systems (Hu *et al.*, 1998). In regime I, which occurs below a critical stress σ_c (and shear rate $\dot{\gamma}_c$), a fluid phase (FP) is observed in which shear flow tends to align the wormlike micelles. In regime II, which occurs for stresses $\sigma_c < \sigma < \sigma_s$, the FP and a viscous phase of shear-induced structures (SISs) coexist. In regime III, which occurs for stresses $\sigma_s < \sigma < \sigma_f$, the gap is saturated with SISs which, as we shall see, flow as a plug with slip at the walls of the flow cell. In regime IV, which occurs for stresses above σ_f, the SIS exhibits mechanical failure followed by flow instabilities.

In this article, we investigate the rheological behavior of regimes III and IV in detail. We explore a range of concentrations, from 1.0 to 10 mM, over which shear thickening is observed. The article is organized as follows: after reviewing sample preparation and experimental apparatus, we present the rheological properties for the solutions near equilibrium and prior to shear thickening (Sec. III A). We then present rheological data under strong flow where shear thickening is observed (Sec. III B). We show that wall slip occurs in the shear-thickened state (Sec. III C). This allows us to account for some of the geometry-dependent rheology reported in the literature [Ohlendorf *et al.* (1986); Brunn and Wunderlich (1989); Hu and Matthys (1995)]. We then present rheological and visualization results which show that the SIS fracture above a concentration-dependent shear stress. Finally, in Sec. IV, we discuss our results in light of the previous experiments.

II. EXPERIMENT

A. Materials

The surfactant system investigated in this study is the same as that described in the preceding paper (Hu *et al.*, 1998). The tracers used in velocity profile measurements described in Sec. III C 2. were mica particles (Mearlin superfine, Mearl Corporation).

B. Instrumentation

Two sets of apparatus were used for simultaneous visualization and rheological measurements. The first apparatus consisted of a Rheometrics DSR controlled-stress rheometer with various custom made transparent Couette flow cells and a light scattering microscopy setup. This apparatus is described in the preceding paper (Hu *et al.*, 1998). One drawback of the stress-controlled rheometer is that it may take up to 15 s after startup for it to reach the desired stress, depending on the viscosity of the solution. Thus, the initial part of the transients obtained with the controlled-stress rheometer is not always reliable. However, since the times required for the samples to shear thicken and reach a steady state are typically 10^2-10^4 s, this is not a severe limitation. The second apparatus used was similar to the first, except that the DSR rheometer was replaced with a Rheometrics ARES controlled-strain-rate rheometer with its own transparent Couette flow cells. This setup allows accurate transient controlled-strain-rate experiments to be performed.

TABLE I. Flow geometries.

Instrument	Geometry	Reference name	Bob diameter (mm)	Cup diameter (mm)	Gap (mm)	Bob length (mm)	Cone angle (rad)
	Coni-cylinder	CON32	32.0	34.0	1.0	32.3	0.040
ARES	Couette	COU32	32.0	34.0	1.0	33	—
	Couette	COU23.5	23.5	25.9	1.2	30	—
	Couette	COU29.5	29.5	32.0	1.25	44	—
	Couette	COU24.9	24.9	25.9	0.5	55	—
DSR	Couette	COU24.5	24.5	25.9	0.7	55	—
	Couette	COU23.5	23.5	25.9	1.2	55	—
	Couette	COU21.9	21.9	25.9	2.0	55	—
	Couette	COU42.8	42.8	50.8	4.0	30	—
RMS800	Coni-cylinder	CON50	50.0	52.0	1.0	20	0.040

In addition, a Rheometrics RMS800 rheometer was used for some of the rheological characterizations to give us an additional flow cell of different size. A number of different flow cells were used in this study; their dimensions are listed in Table I. Experiments were performed at $22.5 \pm 0.3\,^{\circ}\mathrm{C}$.

III. RESULTS

A. Properties near equilibrium and prior to shear thickening

The dynamic viscosity of our micellar solutions is strongly concentration dependent. This is illustrated in Fig. 1(a) where we plot the magnitude of the complex viscosity $|\eta^*(\omega)|$ as a function of angular frequency for several different concentrations. Essentially the same concentration dependence is exhibited in the ''induction'' viscosity $\eta_I(\dot{\gamma})$ as a function of shear rate. (The ''induction'' viscosity $\eta_I(\dot{\gamma})$ is the viscosity measured during the period prior to the shear-induced increase in the apparent viscosity of the solution. For shear rates less than the critical shear rate, this corresponds to the steady state viscosity.) These measurements represent solution properties in the absence of any shear-induced structures. Note that the zero-shear-rate viscosity η_0 varies by more than a factor of 1000 for these solutions. The overlap concentration c^* is approximately 3.3 mM, since at that concentration, the solution has a zero-shear-rate viscosity which is approximately twice the solvent (water) viscosity [Hu and Matthys, (1996)]. The absence of shear thinning for concentrations below 3.3 mM is consistent with the assignment of $c^* \cong 3.3$ mM. As we shall see, shear thickening is observed for solutions with concentrations both above and below c^*, over the entire range of concentrations from 1 to 10 mM.

The storage and loss moduli $G'(\omega)$ and $G''(\omega)$ are similar to those shown in the previous paper [Fig. 3(b)] over the concentration range studied (5–10 mM). Cole–Cole plots of the data do not follow a semicircle indicating that the dynamic moduli do not exhibit simple Maxwell behavior. Above concentrations of approximately 20 mM, twice that of the highest concentration used in this study, Maxwell behavior is recovered [Cates and Candau (1990)].

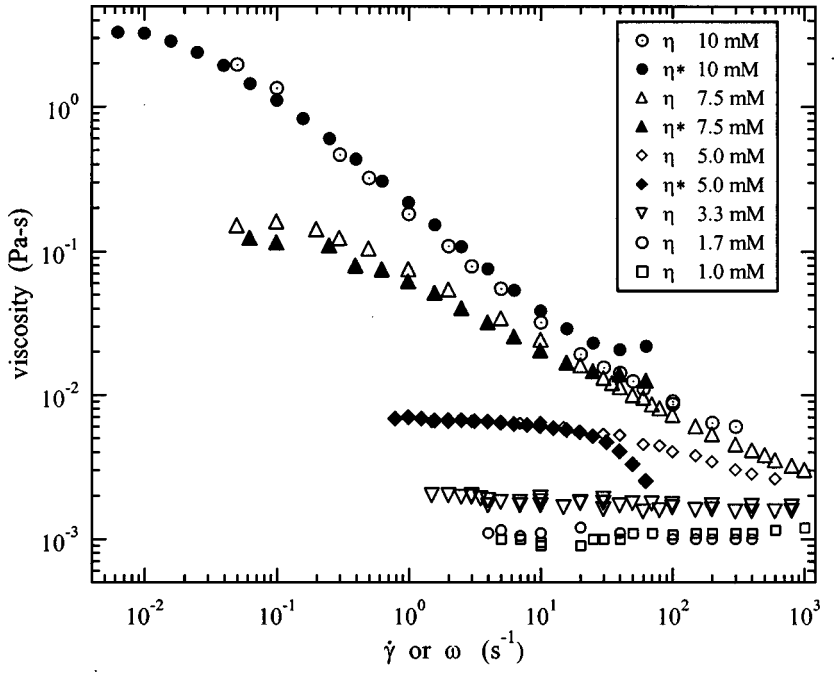

FIG. 1. Initial steady flow viscosity η_0 prior to the onset of shear thickening and the magnitude of the dynamic complex viscosity $|\eta^*(\omega)|$ for equimolar solutions of TTAA/NaSal under different concentrations (flow cell: COU32).

B. Typical rheological behavior under strong flow

Typical transient rheological behavior under strong flow is shown in Fig. 2 where we plot the apparent viscosity as a function of time in response to the sudden application of a constant shear rate (a) or a constant shear stress (b) to an equimolar 1.7/1.7 mM NaSal/TTAA solution. (As we shall see, the flow in the shear-thickened state is inhomogeneous. Therefore, we refer to the viscosity calculated by dividing the measured stress by the average shear rate as an ''apparent'' viscosity.)

Figure 2 shows the three regimes characteristic of a time-dependent shear-thickening fluid: induction, growth, and plateau. All three regimes are observed under conditions of controlled shear rate, shown in Fig. 2(a) and controlled shear stress, shown in Fig. 2(b). Note that the ''induction'' viscosity for this solution is about the same as the solvent (water), whereas the plateau viscosity is about 35 times higher. For the controlled shear stress measurements, the shear rate is not constant in time but has a time dependence which is inversely proportional to the apparent viscosity, as shown by the lighter curve in Fig. 2(b). Note that the steady state apparent viscosity exhibits noticeable temporal fluctuations for both types of measurements. This is typical of data in regime III.

In Fig. 3, we show the steady state rheological behavior for a 1.7/1.7 mM TTAA/NaSal solution. We plot the data two ways: as the shear stress versus apparent shear rate in Fig. 3(a) and as an apparent viscosity versus apparent shear rate in Fig. 3(b). Similar curves were obtained at all concentrations (e.g., see Fig. 15 of the previous article, Part I). We delineate the four regimes of rheological behavior in each of these figures. The four regimes are defined by critical shear stresses σ_c, σ_s, and σ_f. In regime I ($\sigma < \sigma_c$), the stress rises with increasing shear rate. For $c < c^*$, the viscosity is inde-

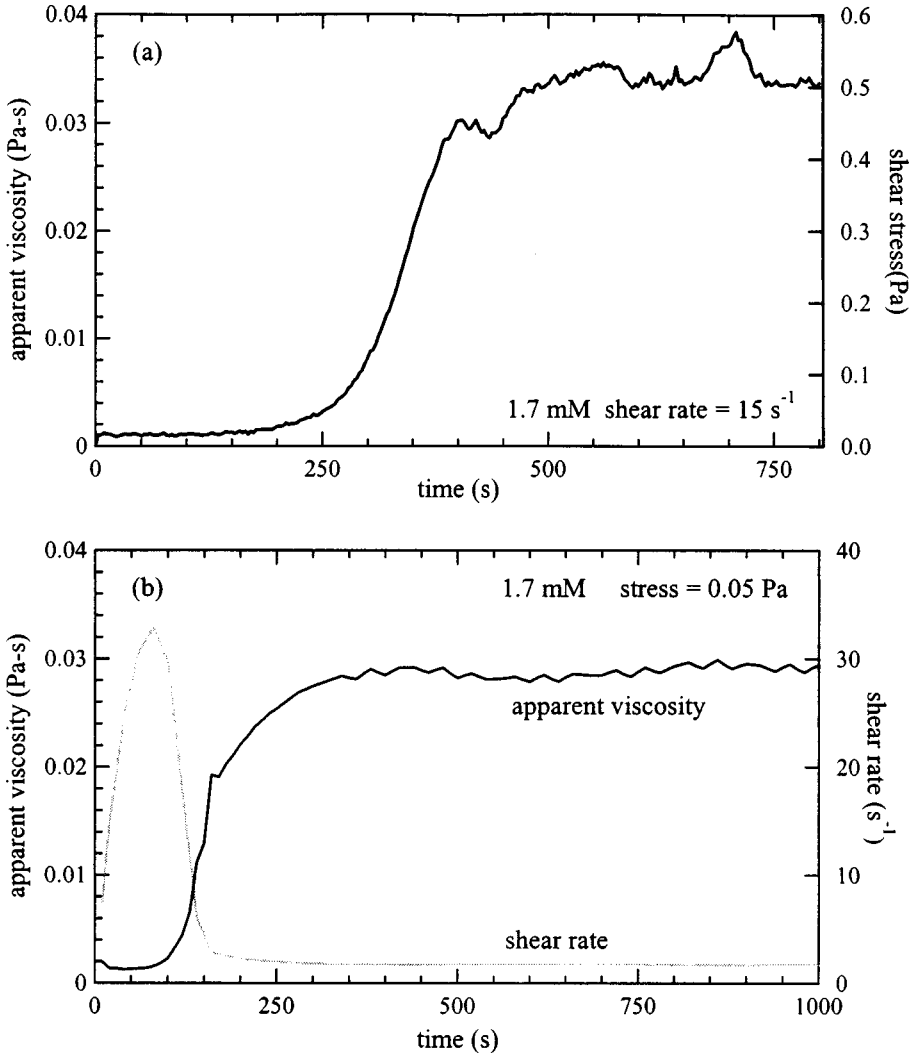

FIG. 2. (a) Apparent viscosity as function of time after the commencement of shear flow for a constant shear rate of 15 s^{-1}. The induction period corresponds to the time up to about 150 s; the growth period corresponds to the time between approximately 150 and 500 s; the plateau period corresponds to the time after about 500 s (flow geometry: CON32). (b) Apparent viscosity (dark line) and shear rate (gray line) as function of time after the commencement of shear flow for a constant applied stress of 0.05 Pa (flow geometry COU29.5).

pendent of shear rate (to within the uncertainty of our measurements), and for $c > c^*$, the viscosity decreases with shear rate. The sheared solution in regime I consists of a micellar FP; this phase differs from the equilibrium phase primarily in that the micelles are partially aligned by the flow. In regime II ($\sigma_c < \sigma < \sigma_s$), the shear rate first decreases and then increases with increasing shear stress. SISs nucleate inhomogeneously at the inner wall of the Couette cell (for start-up experiments in which the stress or shear rate is increased abruptly from zero) and coexist in steady state with the FP (Hu *et al.*, 1998). In regime III ($\sigma_s < \sigma < \sigma_f$), the shear stress varies approximately linearly with shear rate in regime III such that the system exhibits a nearly constant apparent viscosity. The SISs nucleate homogeneously and fill the gap of the Couette cell

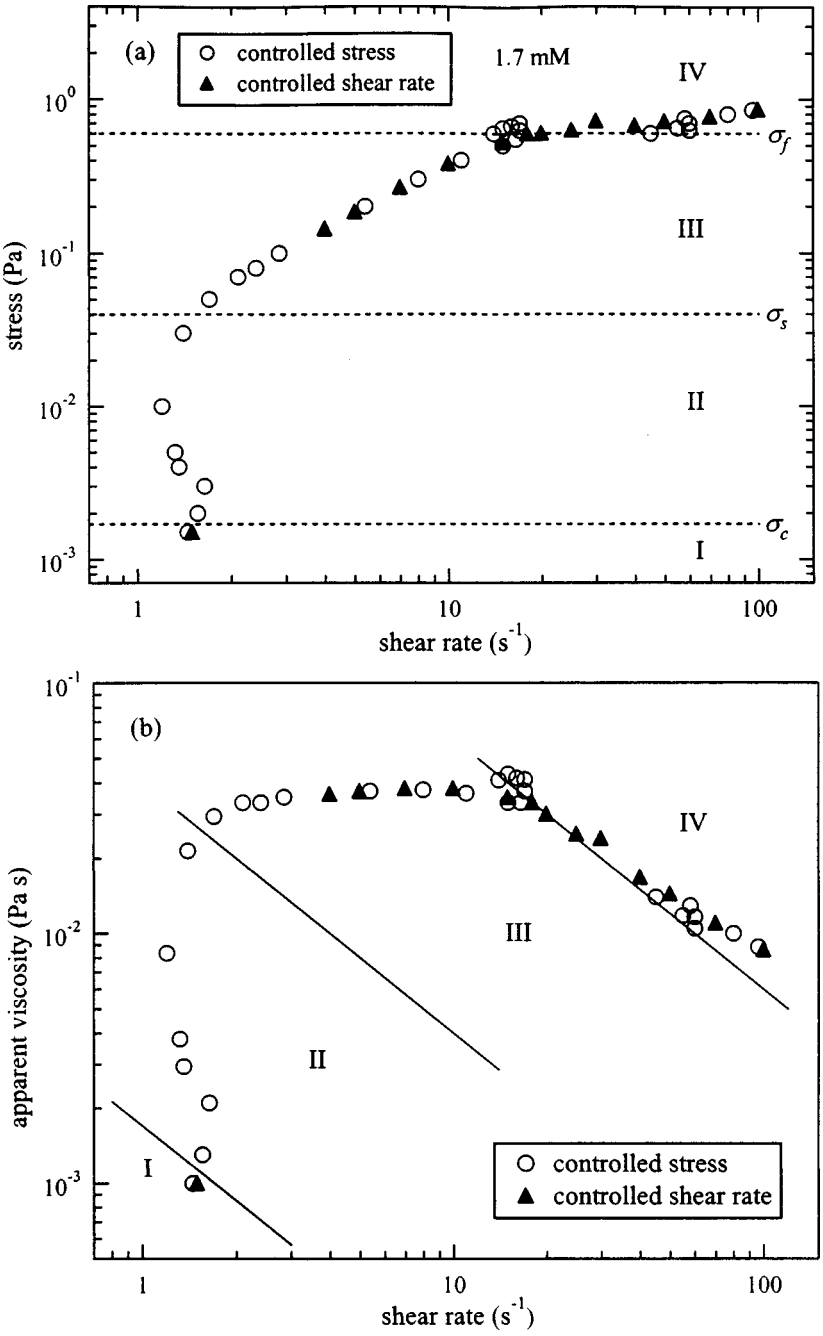

FIG. 3. Steady state rheological behavior of 1.7/1.7 mM TTAA/NaSal surfactant solution. (a) Steady state stress vs shear rate and (b) steady state apparent viscosity vs shear rate (flow geometry: COU29.50).

(for start-up experiments). In regime IV ($\sigma > \sigma_f$), the stress exhibits a plateau and the apparent viscosity decreases with shear rate.

Transient and steady state results were obtained for other surfactant concentrations between 1 and 10 mM. The systems all show similar qualitative features except for the

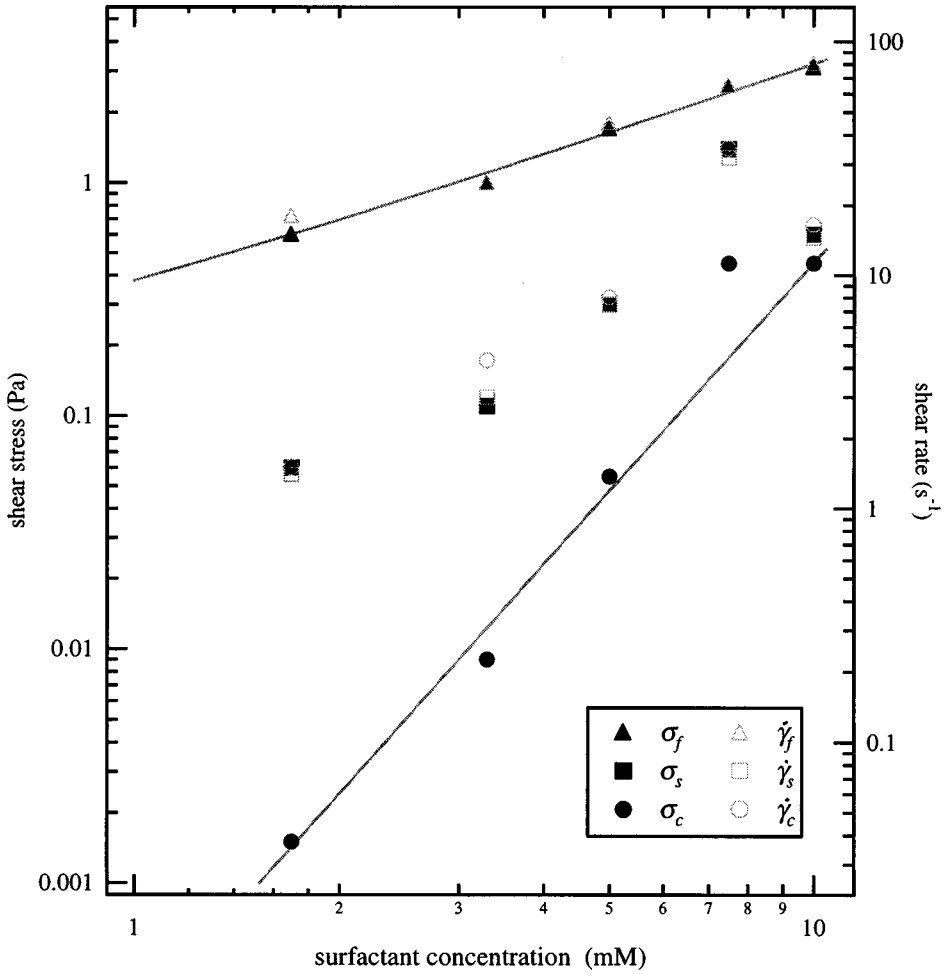

FIG. 4. Values of the critical shear stresses (closed symbols) and shear rates (open symbols) as a function of surfactant concentration. The critical shear stress σ_c for the onset of shear thickening increases with a power of about 3.2 with concentration. The critical shear stress σ_f (and rate $\dot{\gamma}_f$) for fracture of the SIS increases linearly with concentration.

variation of critical stresses and shear rates with concentration. Figure 4 shows these critical values as a function of the surfactant concentration. In this graph, the scales for the axes are chosen so that the curves for shear rate and stress superpose. It should be noted that $\dot{\gamma}_c$ and $\dot{\gamma}_s$ are about the same, which is why the $\dot{\gamma}_c$, $\dot{\gamma}_s$, and σ_s curves are essentially superposed. The lines through the data for σ_f and σ_c have slopes of 1.0 and 3.2, respectively, indicating that σ_f has a linear concentration dependence and that σ_c has approximately a cubic concentration dependence.

C. Rheological behavior in regime III

1. Concentration-independent plateau viscosity

In Fig. 5, we show the transient apparent viscosity as a function of strain (i.e., shear rate multiplied by time) for various surfactant concentrations under controlled rate flow in regime III. It is remarkable that all samples exhibit the same plateau apparent viscosity

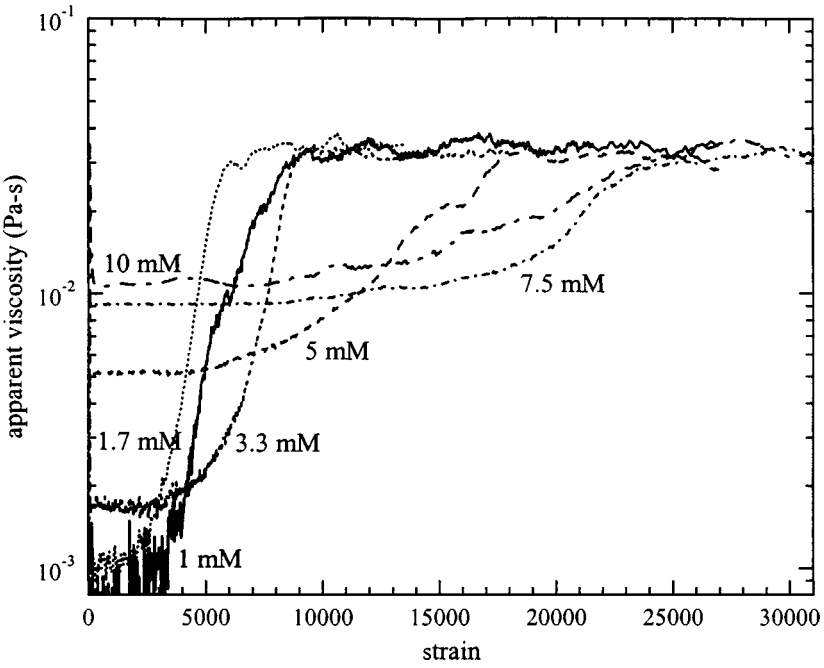

FIG. 5. Transient viscosity plotted against total strain (shear rate multiplied by time) for different concentrations. Note the vastly different viscosities at $t = 0$ and apparently identical viscosities at long times. All the curves are taken from regime III (flow geometry: CON32).

even though they have very different concentrations and start out with vastly different (induction) viscosities. For each sample in Fig. 5, the shear rate was chosen so that the steady state corresponded to regime III (thus, the shear rates are 5, 10, 12, 15, and 40 s^{-1} for the 1, 1.7, 3.3, 5, 7.5, and 10 mM solutions, respectively).

To further explore the rheological behavior of regime III, in Fig. 6 we plot the apparent viscosity and steady state stress as a function of shear rate for regimes III and IV at all concentrations. Data were measured under both controlled shear rate and controlled shear stress using the same flow cell on the DSR rheometer. Figure 6 clearly shows that the plateau apparent viscosity in regime III is independent not only of shear rate but also concentration. To appreciate the significance of these data, it should be noted that the near-equilibrium (''induction'') viscosities for these solutions vary from 0.001 Pa s for the 1 mM solution to 3.3 Pa s for the 10 mM solution, i.e., over more than 3 decades of viscosity. Nevertheless, all these samples exhibit the same steady state apparent viscosity over a wide range of shear rates.

2. Velocity profile

The key to understanding the concentration-independent viscosities in regime III lies in understanding the spatial variations of the flow field in this regime. Accordingly, we measured the velocity profiles in the gap of the Couette cells. To obtain these velocity profiles, we illuminated the gap of a transparent Couette cell with a sheet of laser light that was perpendicular to the rotation axis. Small mica particles were added to the fluid, and a movie of the region illuminated by the laser sheet was collected by a charge coupled device (CCD) camera and recorded on a VCR. The illuminated particles in the gap of the Couette cell could then be seen on successive video images separated by 1/30

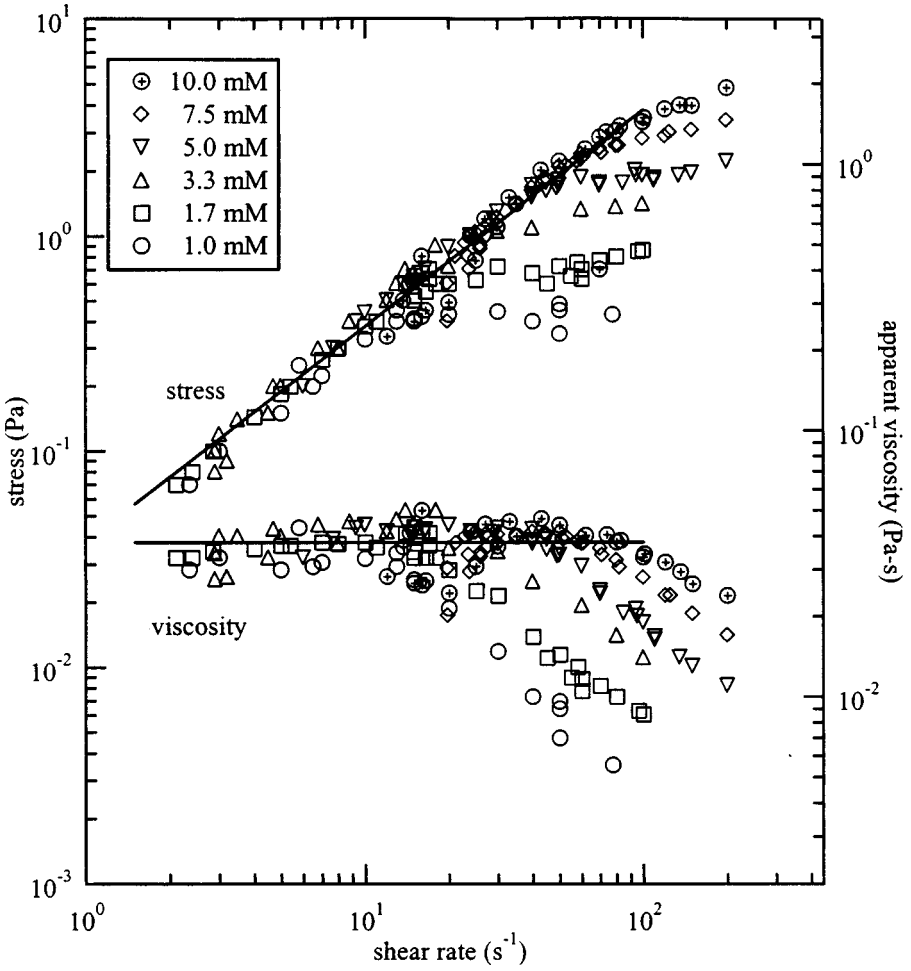

FIG. 6. Apparent viscosity and stress in regimes III and IV vs shear rate (flow geometry: COU29.5). Note that all samples have approximately the same apparent viscosity in regime III, as indicated by the solid line. Sample: 1–10 mM equimolar TTAA/NaSal solutions.

s in time. The measured displacement of the particles between frames allows us to measure their velocity, although the frame speed limitation of the camera limits the shear rate over which this technique is suitable. To facilitate these measurements, we used a sample with a low surfactant concentration (1.7/1.7 mM TTAA/NaSal) since it has a relatively small critical shear rate. We also used a flow cell with a large gap (4 mm, COU42.8 tool) to improve spatial resolution.

Representative velocity profiles are shown in Fig. 7 for a typical experiment in which a constant finite shear rate $\dot{\gamma} = 1\ \mathrm{s}^{-1}$ is applied to a well-rested sample. (In this case the inner wall is moving and the outer wall is at rest. The velocities of the walls are shown by the data on the borders of the graphs.) Immediately after the inner cylinder starts to move, the familiar linear velocity profile for a homogeneous shear flow is observed, as shown in Fig. 7(a). As the SIS begins to grow from the inner surface, we see a progressively thicker region of uniform velocity developing, with a steeper velocity gradient region near the outer cylinder, as illustrated by the profile shown in Fig. 7(b) at 438 s. After 735 s, we see in Fig. 7(c) that the SIS is still attached to the inner wall (i.e., there

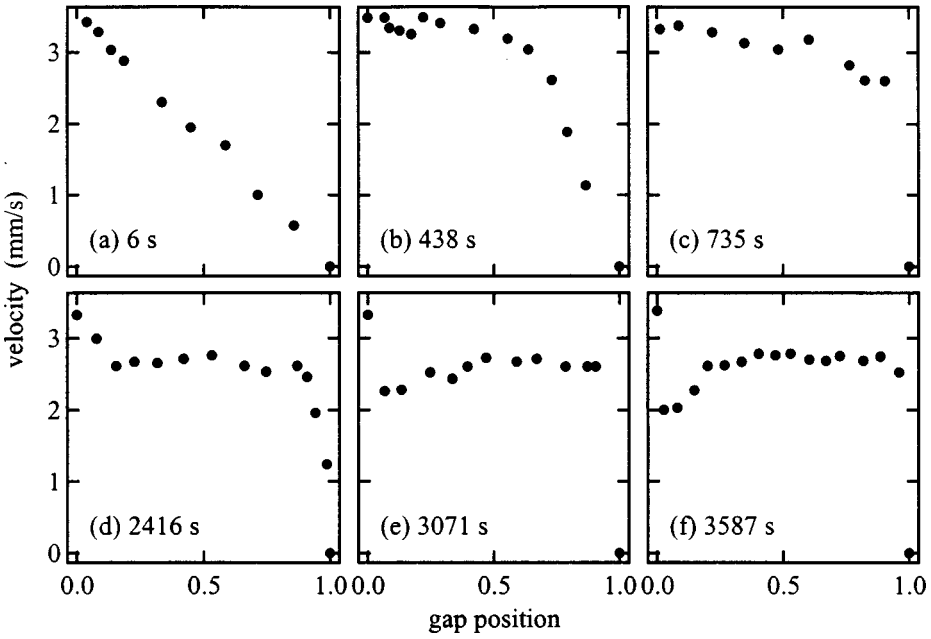

FIG. 7. Time development of the velocity profile in the gap of the flow cell for $\dot{\gamma} = 1\,s^{-1}$ for a 1.7/1.7 mM NaSal/TTAA solution. The coordinates are referenced to the inner cylinder (gap position 0.0) and the outer cylinder (gap position 1.0) (flow geometry: COU42.8).

is a thick region next to the inner cylinder which is moving with nearly the same velocity as the inner cylinder) and that there is a thin layer near the outer wall in which a large velocity gradient exists. After 2416 s, the velocity shown in Fig. 7(d) is uniform over most of the gap, but an additional thin layer with a large velocity gradient develops near the inner wall. At even later times, shown in Figs. 7(d)–7(e), we see that the velocity has become approximately uniform over most of the gap, except in two thin layers of fluid near the inner and outer walls which account for most of the velocity gradient. Thus, the SIS fills most of the center of the gap and behaves as a ''solid'' body in rotation, accompanied by two narrow layers next to the inner and outer cylinders undergoing significant shear to accommodate the no-slip conditions at the walls. For simplicity, we refer to these two narrow layers as ''slip'' layers hereafter. (Note that in some cases we observed slip only at the outer wall.) The high rate of shear in these slip layers suggests that the fluid in these layers has a much lower viscosity than the SIS in the bulk. This picture is consistent with the notion of the SIS being a ''quasisolid'' or ''very high viscosity'' gel phase, as discussed in our previous article. These observations can be used to understand why the apparent viscosity in regime III is not concentration dependent, as discussed previously (see Fig. 6).

3. Origin of constant apparent viscosity in regime III

To understand how slip between the SIS and the cell surface can lead to a constant apparent viscosity independent of surfactant concentration and shear rate, we consider a simplified model of the flow field. We divide the gap of width h_0 into two regions: a fluid slip layer of thickness h_f with an average shear rate of $\dot{\gamma}_f$ at the outer surface of the Couette cell, and an SIS layer of thickness $h_0 - h_f$ with an average shear rate of $\dot{\gamma}_{SIS}$ over the remainder of the gap. (As discussed earlier, there can also be two such slip layers, but

the reasoning which follows still applies.) From our measurements of the velocity profile, we know that the velocity difference across the SIS layer is much smaller than the total velocity difference across the gap. In this limit, the apparent viscosity is $\eta_a \approx \eta_f h_0/h_f$. Thus, the observation that η_a is independent of surfactant concentration implies that η_f/h_f is independent of surfactant concentration. To understand how this might come about, we note that the shear rate within the slip layer $\dot{\gamma}_f$ is a factor of h_0/h_f greater than the apparent shear rate $\dot{\gamma}_a$ (or equivalently, the spatially averaged shear rate). A direct examination of Fig. 7 reveals that the slip layers are no thicker than 1/30 of the overall gap, and likely thinner, so that $\dot{\gamma}_f \gg \dot{\gamma}_a$. If $\dot{\gamma}_f$ is sufficiently large, the viscosity η_f of the fluid in the slip layer will be reduced close to that of water (η_w), since the fluid is severely shear thinning (see Fig. 1). (It is also possible that this fluid is depleted of surfactant further reducing its viscosity closer to that of water.) If we assume that the thickness of the slip layer is independent of shear rate and concentration, then the apparent viscosity, $\eta_a \approx \eta_f h_0/h_f$, will be independent of shear rate and surfactant concentration. For our experiments, typical values are $h_0 = 1.2$ mm and $\eta_a \approx 40$ mPa s. Assuming that $\eta_f \approx \eta_w \approx 1$ mPa s, we find the thickness of the slip layer to be $h_f \approx \eta_f h_0/\eta_f \approx 30\,\mu$m. Thus, the average shear rate in the fluid slip layer $\dot{\gamma}_f \approx \dot{\gamma}_a h_0/h_f = 40\dot{\gamma}_a$, which is consistent with our assumption that the fluid in the slip layer(s) is strongly shear thinned. Within this scenario, both η_f and h_f are independent of shear rate and surfactant concentration, which seems to us to be somewhat more likely than only the ratio η_f/h_f being independent of shear rate and surfactant concentration. Nevertheless, our data do not definitively rule out the latter possibility and it remains something of a mystery as to why h_f should be independent of the shear rate and surfactant concentration.

4. Gap effects

Several groups have reported that the steady state viscosity of shear-thickened micellar solutions increase with the thickness of the gap of the flow cell [Ohlendorf *et al.* (1986); Brunn and Wunderlich (1989); Hu and Matthys (1995)]. Brunn and Wunderlich (1989) speculated that this gap effect might be caused by an increase in the size of micellar structures when the gap is increased. We have also observed a significant increase of the apparent viscosity with increasing gap for our samples in the shear-thickened state (regime III). In Fig. 8(a), we show the results of one set of measurements of the apparent viscosity as a function of shear rate using four different gap widths. An approximately fourfold increase in the apparent viscosity as the gap width is increased from 0.5 to 2.0 mm is observed.

Using the results of Sec. III C 3, we can account for this increase using a simple model that does not invoke any microstructural change in the sample as a function of gap width. In Sec. III C 3, we found that the apparent viscosity in the shear thickened state (regime III) is given by $\eta_a \approx \eta_f h_0/h_f$. Assuming, as we did above, that the viscosity η_f and thickness h_f of the fluid slip layer(s) in the steady state do not change for different gaps, this model predicts that the apparent viscosity η_a should be directly proportional to the thickness of the gap h_0. The effective shear rate is just the shear rate in the slip layer, $\dot{\gamma}_f \approx \dot{\gamma}_a h_0/h_f$, and is proportional to the angular velocity Ω of the Couette cell. Therefore, to test our model, we plot η_a/h_0 as a function of the angular velocity Ω in Fig. 8(b). All the data in regime III (and IV) collapse onto one single curve, which confirms our hypothesis. Thus, the gap effect seems to be a consequence of the slipping of the SIS along the walls of the flow cell through a thin lubricating fluid layer. One does not need

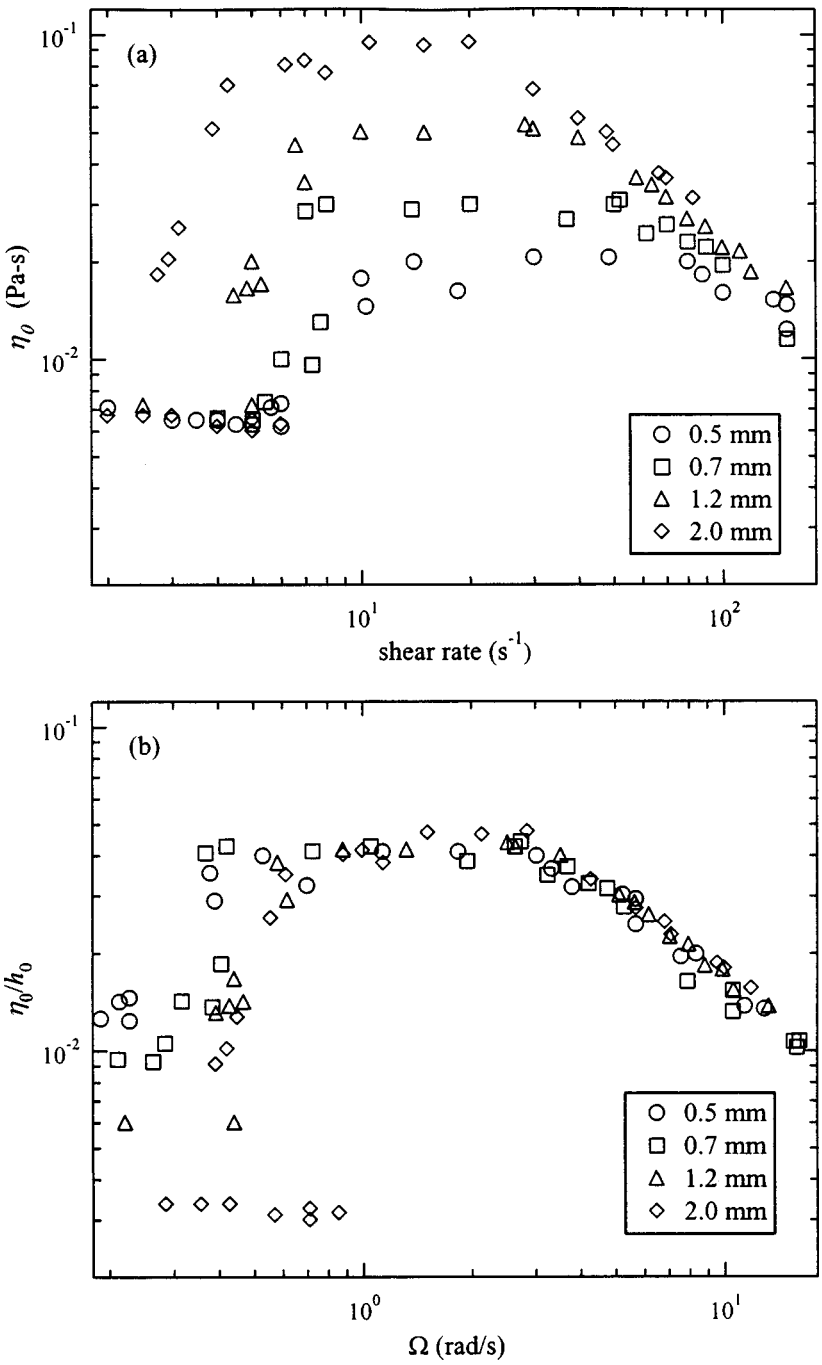

FIG. 8. (a) Steady state apparent viscosity vs shear rate measured for various cell gaps. (b) Scaled data from (a): apparent viscosity normalized by the gap width vs angular velocity Ω of the Couette cell. Flow geometries: COU21.9, COU23.5, COU24.5, COU24.9; Sample: 5/5 mM TTAA/NaSal.

to invoke a change in the characteristic length of the micelles or any other change in the microstructure of the solution to account for the observed gap effect.

The thickness of the gap affects not only the steady state apparent viscosity but also the transient behavior. Hu and Matthys (1995) found that the induction time is approxi

mately inversely proportional to the thickness of the gap for a 5/5 mM TTAA/NaSal solution sheared at 100 s^{-1}. We believe that this dependence may be related to the homogeneous nucleation through which the SISs form in regime III (see previous article, Part I). It is well known that the average nucleation time for a homogeneously nucleating system is inversely proportional to sample volume [Evans and Wennerström (1994)]. This result is simply a consequence of the expectation that the nucleation rate per unit volume should be a constant. The 5/5 mM solution studied previously by Hu and Matthys (1995) was sheared at 100 s^{-1} with an initial stress of 0.43 Pa, which is greater than critical stress σ_s necessary for homogeneous nucleation (0.3 Pa, see Fig. 4). Thus, the inverse dependence of the induction time on gap thickness observed previously by Hu and Matthys (1995) is consistent with the expected inverse dependence of the nucleation time with sample volume.

D. Fracture and instability

The steady state behavior enters another distinct regime (regime IV) when the stress reaches a critical value σ_f. At this point, the stress becomes essentially independent of shear rate and the data exhibit a stress plateau, as illustrated in Fig. 3(a). The appearance of the stress plateau suggests that the sample may have undergone some kind of mechanical failure, such as yielding or fracture. To investigate this possibility, we collected light scattering images of the sample as the stress was increased from a value just below σ_f (regime III) to a value just above σ_f (regime IV). These images were obtained by illuminating the solution in the gap of a transparent Couette cell with a sheet of laser light parallel to the rotation axis and perpendicular to the flow direction, as described in the previous article, Part I (Hu *et al.* 1998). Several light scattering images of the SIS obtained under these conditions are shown in Fig. 9.

In regime III, the SISs in Fig. 9 appear to be densely packed with few droplike irregularities. By contrast, the SISs in regime IV are characterized by long black cracks in the bulk of the sample. These images, coupled with the stress plateau in the rheological data, suggest that when the shear stress exceeds σ_f, the SIS fails by cracking in the bulk. The cracking is accompanied by a flow instability which produces the large vortices observed in Fig. 9. To within the temporal resolution of our measurements, the cracking and flow instability appear to occur simultaneously, i.e., we are unable to distinguish which of the two mechanisms occurs first. Nevertheless, it seem most likely that instabilities occur only after the integrity of the SIS is broken by fracture. The fracture then leads to a flow instability driven by the high elasticity of the SIS stretched by the shear cell.

The transient behavior near σ_f is characterized by large temporal fluctuations of the apparent viscosity. Typical fluctuations are illustrated in Fig. 10 for the 1.7/1.7 mM NaSal/TTAA solution. Data for three shear stresses are shown: one above, one below, and one equal to the fracture stress $\sigma_f = 0.7$ Pa. Some fluctuations are already visible in regime III at 0.3 Pa, somewhat below the fracture stress. Note, however, that at the transition from regime III to IV, $\sigma_f = 0.7$ Pa fluctuations become particularly striking, with some exceeding 400%. The apparent viscosity fluctuates on a time scale on the order of many minutes and is characterized by periods of slip near the wall (high apparent viscosity as discussed in the section on regime III) and of fracture as suggested by Fig. 9 (low apparent viscosity). In these measurements, the stress is held constant such that fluctuations in the apparent viscosity correspond to fluctuations in the spatially averaged shear rate. Note that the transient behavior at stresses higher than σ_f exhibit only very small fluctuations as well as a small apparent viscosity. By contrast, the apparent viscosity at or very near σ_f appears to oscillate between the high apparent viscosity of regime

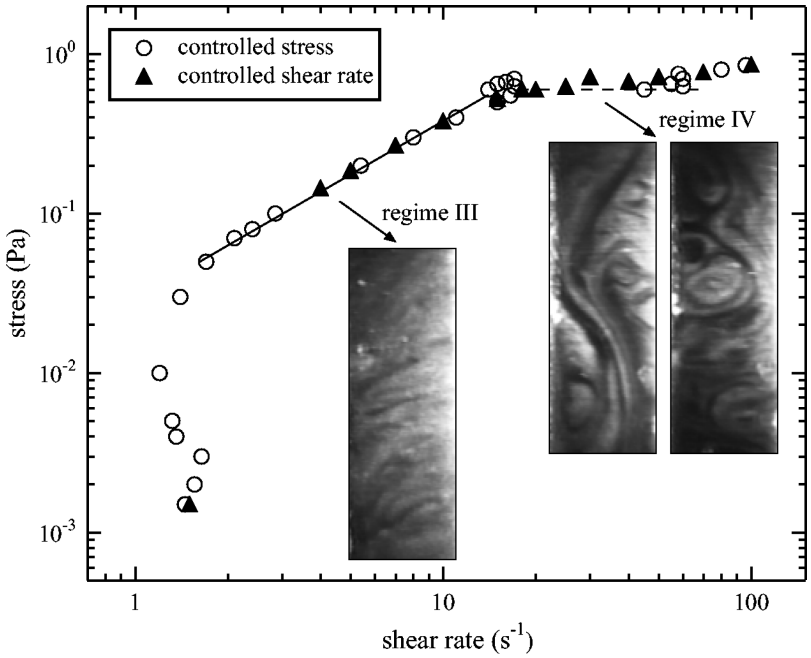

FIG. 9. SIS images corresponding to regime III and regime IV for a 1.7/1.7 mM NaSal/TTAA solution, and corresponding shear stress/shear rate data (flow geometry: COU23.5).

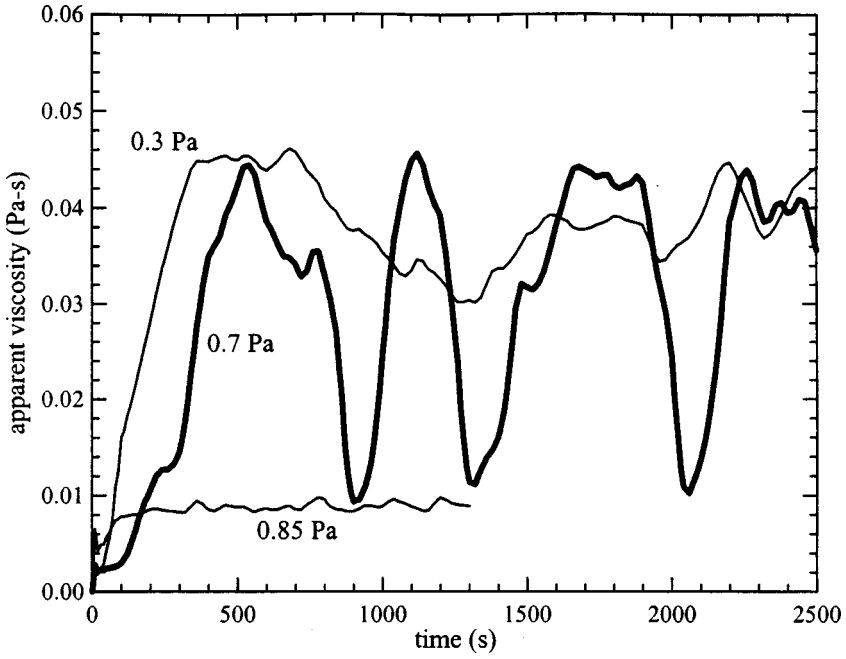

FIG. 10. Time evolution of apparent viscosity at stresses below (0.3 Pa), near (0.7 Pa), and above (0.85 Pa) the fracture stress for a 1.7/1.7 mM NaSal/TTAA solution (flow geometry: COU23.5). Note the very large fluctuations for a stress of 0.7 Pa (bold curve) near the fracture stress.

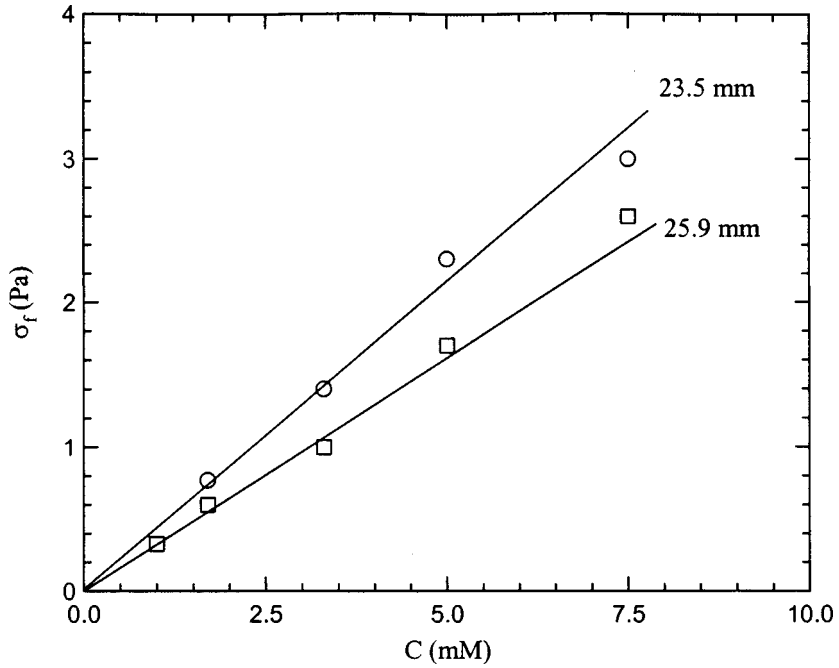

FIG. 11. Fracture stress as a function of concentration for two different cell diameters. For a given cell diameter, the fracture stress increases linearly with surfactant concentration. The fracture stress seems to decrease, however, when the cell diameter is increased (flow geometries: COU29.5, COU23.5).

III and lower apparent viscosity of regime IV. This can be seen not only for the data taken at σ_f in Fig. 9, but can also be seen in Fig. 3 where the data obtained near σ_f are clustered about two shear rates, one near $\dot{\gamma} = 15\ s^{-1}$ (corresponding to the high apparent viscosity state) and the other near $\dot{\gamma} = 55\ s^{-1}$ (corresponding to the low apparent viscosity state). The data suggest that there is a dynamic alternating transition between these two states.

The fracture stress σ_f increases linearly with surfactant concentration, as illustrated in Fig. 11, indicating that the strength of the gellike structures increases with surfactant concentration. This seems quite reasonable if one assumes that micelles are linking up in some way to form larger structures so that the number of links or ''bonds'' per unit volume is proportional to the concentration. One puzzling feature of these data, however, is that the fracture stress σ_f also seems to vary inversely with the diameter of the cell. This is illustrated in Fig. 11, where we show σ_f versus surfactant concentration for two different cell radii, and in Fig. 12, where we show σ_f versus the cell diameter D for four different concentrations (the cell gap is between 1.0 and 2.0 mm in all cases). We do not understand the origin of this behavior. Note that the diameter is varied between approximately 24 and 50 mm and that the gap in all cases is between 1.0 and 2.0 mm, which is much smaller than the diameter. It is also useful to point out that the shear stress is not strictly uniform across the gap in a Couetter cell but decreases inversely as the square of the radius. (This is dictated by mechanical equilibrium which requires that the net torque on a fluid or solid element be zero when there is no angular acceleration. Note also that the stress we cite is the stress at the inner cylinder of the constant stress rheometer.) It may be that the inhomogeneity of the stress leads to an inhomogeneity of the gel phase

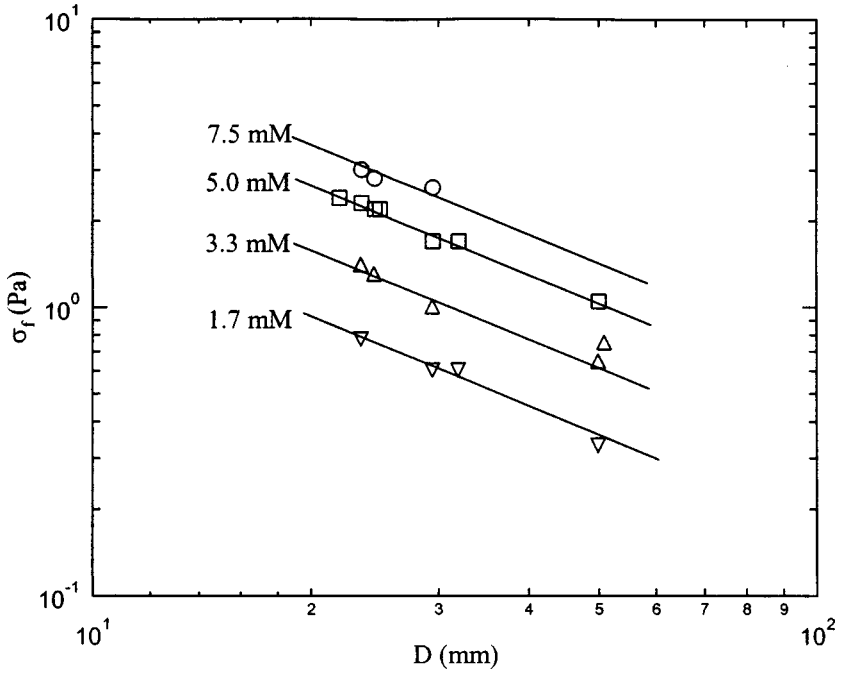

FIG. 12. Fracture stress as a function of inner cylinder diameter for four different surfactant concentrations. The solid lines have a slope of -1. (Flow geometries: COU21.9, COU23.5, COU24.5, COU24.9, COU29.5, COU32, COU50).

and an apparent dependence of the fracture stress on the diameter of the cell. Further investigation is required to understand this puzzling result.

IV. DISCUSSION

Shear thickening is generally observed in wormlike micellar systems consisting of very long micelles at concentrations near the overlap concentration. In the experiments reported in this work, the overlap concentration is 3.3 mM and shear thickening is observed from 1 to 10 mM. Upon the commencement of shear flow, the micelles align and are stretched [Wunderlich *et al.* (1987); Hu *et al.* (1993); Hu and Matthys (1996); Liu and Pine (1996)]. For controlled shear rate, this is accompanied by an overshoot in shear stress σ [Hu *et al.* (1993)] and birefringence. Over a considerable time, corresponding to 10^3-10^4 strain units, there is little significant change in shear and normal stress, birefringence, and light scattering images [Boltenhagen *et al.* (1997)]. In addition to aligning with the flow, the mean length of individual micelles may increase, since the shear-induced stretching reduces the configurational entropy and thereby lowers the entropic penalty associated with micellar growth. This stage corresponds to the induction period during which the micelles remain partially aligned with the flow. If the stress is below concentration-dependent shear stress σ_c, the system remains in this state indefinitely.

If the stress is greater than σ_c, the apparent viscosity grows and micelles start to form much larger structures comparable to and eventually much larger than the wavelength of light, as indicated by various light scattering experiments [Liu and Pine (1996); Wheeler *et al.* (1996); Boltenhagen *et al.* (1997)]. These structures are strongly aligned with the

shear flow as evidenced by their strong flow birefringence [Wunderlich *et al.* (1987); Hu *et al.* (1993); Hu and Matthys (1996)] and highly anisotropic neutron and light scattering patterns [Bewersdorff *et al.* (1986); Kalus *et al.* (1989); Hofmann *et al.* (1991); Munch *et al.* (1993); Liu and Pine (1996)]. The structures tend to start growing either at the surface of the Couette cell (regime II behavior), or if the stress is sufficiently high (regime III behavior), in the bulk through a homogeneous nucleation process. In the latter case, it appears that isolated ''droplets'' of the SIS form, grow, and eventually interconnect to form a network (the SIS) with a much higher viscosity than the original micellar solution.

While we do not know the microstructure of the SIS, there is some evidence from light scattering data that individual micelles may aggregate to form bundles [Liu and Pine (1996)]. It is also possible that the SISs consist of interconnected bundles or aggregates of interconnected bundles. This picture is consistent with the highly anisotropic light scattering and strong birefringence of the SIS. A number of other structures have also been proposed, including rodlike micelles with nematic [Hofmann *et al.* (1991)] or even hexagonal ordering [Kalus *et al.* (1989)]. In any case, the concentration of surfactant within the SIS must exhibit large fluctuations on length scales comparable to the wavelength of light since the SIS scatters light much more strongly than the equilibrium solution.

It is significant that the SIS remain intact under an applied shear *stress* even through there is very little flow within the SIS in the fully developed steady state (see Fig. 7). That is, the only significant velocity gradients that exist are confined to a very thin region near the walls of the flow cell and the velocity gradient within the SIS is nearly zero. Thus, it is the shear stress and not the shear rate that is important in maintaining the SIS. This is corroborated by the observation that it is only when the shear stress is reduced below the critical stress that the SIS begin to disintegrate. Thus, it seems that collisions between micelles do not play an essential role in maintaining the SIS, as suggested in some models of shear thickening [Wang (1990); Bruinsma *et al.* (1992)]. Collisions are likely to be important, however, in kinetics of the formation of the SIS. Nevertheless, at this time very little is known about the microstructure of the SIS other than to say that it consists of structures highly aligned with the flow field.

V. SUMMARY AND CONCLUSIONS

In the previous article, Part II, we discussed the formation of SISs in a shear flow. In the present article, we focused on rheological studies of the shear-thickening state in regime III and IV. In regime III, we found the apparent viscosity to be remarkably independent of both shear rate and concentration. Using velocity profile measurements, we found that a large SIS plug nearly occupies the entire gap, with thin slip layers near the walls consisting of low viscosity fluid. We found that the invariance of the apparent viscosity can be explained by the plug flow of the SIS. Using this same model, we could also understand the dependence of the apparent viscosity on the Couette cell gap width.

In regime IV, we observed the SIS fracture at a concentration-dependent stress σ_f, which leads to a constant stress and a decrease in the apparent viscosity as the shear rate is increased. At the transition between regimes III and IV, there are large oscillations in the apparent viscosity which arise from slipping at the walls or fracture of the bulk SIS. The fracture stress is proportional to the concentration and inversely proportional to the cell radius.

In this work, we have used simultaneous rheological and visualization measurements to generate new insights into shear thickening in low-concentration wormlike micellar

solutions. These measurements have revealed previously unknown features of the thickening of surfactant solutions in shear cells and have explained several puzzling previous observations, such as the gap-width effect and the viscosity invariance with concentration and shear rate. Our results provided us with a clearer physical picture of surfactant solution thickening, by explaining some of the experimental artifacts which have confused and obscured our understanding of these systems. We hope that these measurements can be useful in developing an understanding of the stress-induced structural changes in these systems which result in shear thickening.

ACKNOWLEDGMENTS

The authors thank Peter Olmsted and Rachid Makhloufi for useful discussions and Jennifer Politsch for a critical reading of the manuscript. This work was supported by the National Science Foundation under Award Nos. DMR96-32716 (MRL program) and NSF DMR96-25856 (Instrumentation for Materials Research Program).

References

Bewersdorff, H.-W., B. Frings, P. Lindner, and R. C. Oberthur, ''The conformation of drag reducing micelles from small-angle-neutron-scattering experiments,'' Rheol. Acta **25**, 642–646 (1986).

Boltenhagen, P., Y. T. Hu, E. F. Matthys, and D. J. Pine, ''Inhomogeneous structure formation and shear-thickening in worm-like micellar solutions,'' Europhys. Lett. **38**, 389–394 (1997).

Bruinsma, R., W. M. Gelbart, and A. Ben-Shaul, ''Flow-induced gelation of living (micellar) polymers,'' J. Chem. Phys. **96**, 7710–7727 (1992).

Brunn, P. O. and A. M. Wunderlich, ''The complex rheological behavior of an aqueous cationic surfactant solution investigated in a Couette-type viscometer,'' Colloid Polym. Sci. **267**, 627–636 (1989).

Cates, M. E. and S. J. Candau, ''Statics and dynamics of worm-like surfactant micelles,'' J. Phys.: Condens. Matter **2**, 6969–6992 (1990).

Evans, D. F. and H. Wennerström, *The Colloidal Domain: Where Physics, Chemistry, Biology, and Technology Meet* (VCH, New York, 1994).

Hofmann, S., A. Rauscher, and H. Hoffmann, ''Shear induced micellar structures,'' Ber. Bunsenges. Phys. Chem. **95**, 153–164 (1991).

Hu, Y. T., P. Boltenhagen, and D. J. Pine, ''Shear-thickening in low-concentration solutions of worm-like micelles. I: Direct visualization of transient behavior and phase transitions,'' J. Rheol. **42**, 1185 (1998), preceding paper.

Hu, Y. T. and E. F. Matthys, ''Characterization of micellar structure dynamics for a drag-reducing surfactant solution under shear: Normal stress studies and flow geometry effects,'' Rheol. Acta **34**, 450–460 (1995).

Hu, Y. T. and E. F. Matthys, ''The effects of salts on the rheological characteristics of a drag-reducing cationic surfactant solution with shear-induced micellar structures,'' Rheol. Acta **35**, 470–480 (1996).

Hu, Y. T., S. Q. Wang, and A. M. Jamieson, ''Rheological and flow birefringence studies of a shear-thickening complex fluid—A surfactant model system,'' J. Rheol. **37**, 531–546 (1993).

Kalus, J., H. Hoffmann, S.-H. Chen, and P. Lindner, ''Correlations in micellar solutions under shear: A small-angle neutron scattering study of the chain surfactant *N*-hexadecyloctyldimethylammonium bromide,'' J. Phys. Chem. **93**, 4267–4282 (1989).

Liu, C.-H. and D. J. Pine, ''Shear-induced gelation and fracture in micellar solutions,'' Phys. Rev. Lett. **77**, 2121–2124 (1996).

Munch, C., H. Hoffmann, K. Ibel, J. Kalus, G. Neubauer, U. Schmelzer, and J. Selbach, ''Transient small-angle neutron scattering experiments on micellar solutions with a shear-induced structural transition,'' J. Phys. Chem. **97**, 4514–4522 (1993).

Ohlendorf, D., W. Interthal, and H. Hoffmann, ''Surfactant systems for drag reduction: Physico-chemical properties and rheological behaviour,'' Rheol. Acta **25**, 468–486 (1986).

Wang, S. Q., ''Shear-induced phase transition of living polymers (micelles),'' J. Phys. Chem. **94**, 8381–8384 (1990).

Wheeler, E. K., P. Izu, and G. G. Fuller, ''Structure and rheology of wormlike micelles,'' Rheol. Acta **35**, 139–149 (1996).

Wunderlich, I., H. Hoffmann, and H. Rehage, ''Flow birefringence and rheological measurements on shear induced micellar structures,'' Rheol. Acta **26**, 532–542 (1987).